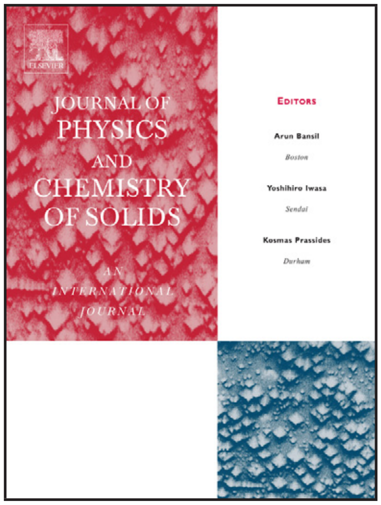

www.elsevier.com/locate/jpcs

Magnetic characterization of $Li_{1+x}Mn_{2-x}O_4$ spinel ($0 \leq x \leq 1/3$)

M. Kopec, J.R. Dygas, F. Krok, A. Mauger, F. Gendron, C.M. Julien

PII: S0022-3697(07)00721-4
DOI: doi:10.1016/j.jpcs.2007.11.005
Reference: PCS 5311

To appear in: *Journal of Physics and Chemistry of Solids*

Received date: 12 January 2007
Revised date: 29 October 2007
Accepted date: 3 November 2007

Cite this article as: M. Kopec, J.R. Dygas, F. Krok, A. Mauger, F. Gendron and C.M. Julien, Magnetic characterization of $Li_{1+x}Mn_{2-x}O_4$ spinel ($0 \leq x \leq 1/3$), *Journal of Physics and Chemistry of Solids* (2007), doi:10.1016/j.jpcs.2007.11.005

Magnetic characterization of $\mathrm{Li}_{1+x}\mathrm{Mn}_{2-x}\mathrm{O}_4$ spinel ($0 \leq x \leq 1/3$)

M. Kopec†, J. R. Dygas†, F. Krok†,

A. Mauger‡, F. Gendron¶, C. M. Julien¶,

†Faculty of Physics, Warsaw University of Technology,

Koszykowa 75, 00-662 Warsaw (Poland)

‡Institut de Minéralogie et de Physique des Milieux Condensés,

Université Pierre et Marie Curie, 140 rue de Lourmel, 75015 Paris (France)

¶Institut des Nano-Sciences de Paris,

Université Pierre et Marie Curie, 140 rue de Lourmel 75015 Paris (France)

PA Classification Numbers: 81.05.-t, 82.45.Vp, 75.50. Pp

Abstract

$Li_{1+x}Mn_{2-x}O_4$ spinels have been prepared by wet route technique in the whole concentration range $0 \leq x \leq 1/3$. Structural analysis has been performed by X-ray diffraction and scanning electron microscopy and Raman spectroscopy. The investigation of impurity phases by magnetic experiments complete the sample characterization, allowing for a comparison with samples obtained by other chemical routes. The analysis of the intrinsic magnetic properties show that the magnetic interactions are Mn^{3+}-O-Mn^{3+} interactions in a geometrically frustrated lattice, while the Mn^{4+}-Mn^{4+} interactions are negligible, with the consequence that the paramagnetic Curie temperature vanishes in the limit $x \simeq 1/3$ where only Mn^{4+} ions remain. A consistent description of both the extrinsic and the intrinsic properties including former investigations of electron paramagnetic resonance has been achieved in relation to the electrochemical properties.

1 Introduction

The lithium manganese spinel $LiMn_2O_4$ is currently the subject of many investigations, since this material is promising for use as positive electrode for advanced lithium-ion batteries [1, 2, 3, 4]. The major difficulty for wide scale applications, however, comes from the difficulty to prepare samples of good quality, because the Jahn-Teller Mn^{3+} ion favors lattice distortions. Cationic substitution in $LiMn_2O_4$ spinel is beneficial to the structural stability of the cubic lattice, because increasing the Mn^{4+} concentration at the expense of the Mn^{3+} concentration avoids both the dilution of electrode and the onset of the Jahn-Teller effect [5]. In this framework, the substitution of Li for manganese according to the chemical formula $Li_{1+x}Mn_{2-x}O_4$, $0 \leq x \leq 1/3$, is associated to a shift of the average valence of the Mn from +3.5 (case $x = 0$) to +4 (case $x = 1/3$). The chemical formula can also be written $Li[Li_xMn_{2-x}]O_4$, to emphasize that the Li^+ ions occupy all the tetrahedral $8a$ sites of the spinel lattice, the part in excess residing on the octahedral positions on the $16d$ sites, in substitution to manganese.

The fragility of the lattice also explains that the structural properties of the material are very sensitive to the mode of preparation. This is evidenced by the different local structure of $Li_{1+x}Mn_{2-x}O_4$ from different sources, investigated in the past by X-ray diffraction [6, 7], electron paramagnetic resonance (EPR) [7, 8, 9, 10], and optical spectroscopy (Raman and Fourier transform infrared spectroscopy) [11]. Different results have been found, depending on the method of preparation of the samples. In particular, a very nice study of the formation of such materials from the reactive system MnO/Li_2CO_3 has been performed by XRD, EPR [6, 7] and nuclear magnetic resonance (NMR) [12]. The result is that such samples with lithium cationic fraction larger than 0.35 prepared by this method are multi-phased, including a stoichiometric phase $LiMn_2O_4$, a non stoichiometric phase $Li_{1+x}Mn_{2-x}O_4$, and the Li_2MnO_3 impurity phase, in addition of the Mn_3O_4 impurity phase. To avoid these impurity phases, wet chemistry has been considered has a promising route to prepare the samples. The EPR characterization of samples prepared by this technique has been performed in [10]. The main features of the EPR spectra are essentially the same, irrespective of the two modes of preparation we have just outlined. In particular, in both cases, the spectra show a sharp line at $x > 0.1$, in addition of the broad asymmetric line observed in nearly stoichiometric ($x<0.05$) samples. The origin of the additional peak, however, is questionable. In samples prepared by the MnO/Li_2CO_3 route, the additional peak has been attributed to the secondary phase Li_2MnO_3 and a sharp line when $x > 0$. This attribution has been questioned by the fact that the peak is observed in samples prepared by the wet chemical route which should avoid the formation of this secondary phase [10]. In addition, the paramagnetic Curie temperature deduced from the values of the Weiss constant was found to remain negative in the whole range $0 \leq x \leq 1/3$, unlike results of direct measurements of the magnetic susceptibility, rising again the question whether this is due to the better accuracy of magnetic measurements, or the difference in synthesis method.

In this context, we found desirable to perform direct magnetic measurements and XRD characterization on samples prepared by the wet chemistry route. We show that the wet chemistry route decreases the proportion of secondary phases with respect to the reactive MnO/Li_2CO_3 route, in agreement with [10], but not to the point than they all disappear as it was suggested in this prior work. The secondary phase $LiMn_2O_4$ is still evidenced in the samples prepared by wet chemistry for x>0.2, but the phase percentage is typically 12 % for $x > 0.25$, against 30% for the same Li excess in samples prepared by the MnO/Li_2CO_3 route. On another hand, the $LiMn_2O_4$ secondary phase is not observed in the Li-rich samples prepared by the wet chemistry route. The presence of Mn_3O_4 impurity phase depends on the sintering temperature. We could detect it for a sintering temperature of 800 ° C, but no longer when decreasing the sintering temperature to 750 ° C.

Another result of this paper concerns the intrinsic magnetic properties of the material. We confirm that the material remains dominated by antiferromagnetic interactions, which vanish in the limit $x = 1/3$ where all the Mn ions are tetravalent. The magnetic properties are dominated by the geometric frustration of these antiferromagnetic interactions in the lattice. This feature is a basic reason why the magnetic properties are very sensitive to the structural properties, with the consequence that the study of the magnetic properties is found to be an efficient tool to probe the crystallinity and structural order at a local scale.

Electrochemical properties show that Mn^{4+} ions are electrochemically inactive and so is the end-member at $x = 1/3$ that contains only manganese in this ionic configuration. This is also the reason for the decrease of the capacity as a function of x from the initial value of 108.7 mAh/g at $x = 0$.

2 Experimental

$Li_{1+x}Mn_{2-x}O_4$ powders with $0.00 \leq x \leq 0.33$ were prepared by the succinic acid-assisted wet chemistry technique [13]. In this technique, the succinic acid plays the role of chelating agent. Stoichiometric amounts of lithium acetate and manganese acetate are dissolved in distilled water. The above solutions are added to aqueous solution of succinic acid (the complexing agent) and heated. The homogeneous precipitates are obtained owing to the poor solubility of manganese and lithium succinates, which are finely dispersed in the solution medium. It is believed that the carboxylic groups on the succinic acid form chemical bond with the metal ions and these mixtures develop the extremely viscous paste-like substance upon slow evaporation of water. The lithium and transition metal cations are trapped homogeneously within the paste and ensure molecular level mixing. The paste is further dried at 110 ° C to obtain the dried precursor mass. The precursor is then allowed to decompose in air at around 400 ° C and heated at 750 ° C. Additionally stoichiometric powder ($LiMn_2O_4$) was heated at 800 ° C, in order to investigate the influence of the sintering temperature.

The structure of $Li_{1+x}Mn_{2-x}O_4$ samples was characterized by the X-ray powder diffraction (XRD) using a diffractometer Philips X'Pert apparatus equipped with a CuKα X-ray source. The diffraction patterns were taken at room temperature in the range $10^\circ \leq 2\theta \leq 80^\circ$ using step scans of 0.0167 ° .

Electrical properties were studied on pressed pellets with gold electrodes sputtered on the polished surface. Impedance measurements were carried out on the Solartron 1260 analyzer from 0.01Hz to 10MHz in the temperature range of 200 ° K to 400 ° K. The impedance spectra are illustrated for two different compositions.

Raman spectra have been measured in the spectral range 200-800 cm^{-1} at room temperature in a quasi-backscattering geometry. A Jobin-Yvon (model U1000)) double monochromator with holographic gratings and a computer-controlled photon-counting system was used. The laser light source was the 514.5 nm line radiation from a Spectra-Physics 2020 argon-ion laser. To have a large signal to noise ratio, 12 successive scans recorded at a spectral resolution of 2 cm^{-1} are averaged.

Magnetic measurements were made on SQUID (Superconducting Quantum Interference Device), using a liquid helium cooled amplifier to measure the magnetic moment in the range from 10^{-7} to 300 emu. Two kinds of measurements were recorded in the temperature range 4 - 300 K : isothermal magnetization $M(H)$ recorded in the field range 0-30 kOe, and temperature dependence of the magnetic susceptibility $\chi(T)$. The magnetic susceptibility was recorded during heating the samples using zero-field cooled (ZFC) and field-cooled (FC) modes at magnetic field 10 kOe. The $\chi(T)$ and $M(H)$ curves were correlated to achieve a complete analysis of the magnetic properties of the materials.

3 Structural properties

3.1 XRD characterization

The XRD diagrams of the $x = 0$ samples display only the cubic spinel phase, and are in agreement with the standard pattern (JCPDS, Card n ° 89-0118). At large values of x, however, the Li_2MnO_3 impurity phase is also detected. The spectra are illustrated at such compositions in Fig. (1). The analysis of the spectra has been performed by Rietveld refinement. The refinement strategy is based on the maximum neighborhood method of Marquardt (Levenberg-Marquardt method [14]), which overcomes the problem of highly correlated parameters in a non-linear least-square refinement. In each cycle, the algorithm optimizes an extra parameter λ that is added to all the diagonal elements in order to improve this usually ill-conditioned matrix. λ is reduced during the refinement to a value between 10^{-3} and 10^{-8}. The results are displayed in Table 1, for both the spinel $Li_{1+x}Mn_{2-x}O_4$ and the monoclinic Li_2MnO_3 impurity phase, when it is detected, i.e. at $x > 0.2$. For $x \leq 0.2$, the amount of this impurity phase is below the detection threshold estimated to few %. Therefore, at any concentration x of Li excess, the amount of this impurity phase is about 2-3 times less than in materials prepared by other chemical route [6, 7]. On another hand, the lattice parameters and volume of the unit cell for this impurity phase, also reported in the Table 1, are found in quantitative agreement with the results reported in these prior works. Therefore, only the amount of this impurity phase is dependent of the mode of preparation, but not its local structure. This is actually expected, because the lattice parameters (and the volume of the unit cell) of this impurity phase are not significantly dependent on x, and close to those of single-phased Li_2MnO_3, so that XRD does not give evidence of any chemical pressure or strain on this impurity phase, coming from its $Li_{1+x}Mn_{2-x}O_4$ environment.

The lattice parameter $a(x)$ of the $Li_{1+x}Mn_{2-x}O_4$ series as a function of x, reported in Fig. (2) shows a large deviation form the linear Vegard's law. This is fully consistent with FTIR experiments [11] , which show that the shift of the stretching frequency of the infrared band as a function of x is not linear, and almost saturates at $x = 1/3$ in x, just like $a(x)$. This rather unusual behavior comes from the fact that an increase of x does not reduce to a chemical pressure effect, which is the implicit condition for obtaining the Vegard's law. It also reduces the amount of Mn^{3+} ions, so that it changes the ionicity of the chemical bonds in the lattice.

The crystallite size was calculated by using Scherrer's formula $\langle L \rangle = k\lambda/(B\cos\theta)$ for the broadening of the spinel (111) and (222) reflections of the $Li_{1+x}Mn_{2-x}O_4$ spectrum with $k = 0.9$ and $\lambda = 1.54056$ Å. The width B of the Bragg peaks due to the size effects has been separated from the broadening associated to the microstrain effects B_{strain} by the different $(\tan\theta)$ dependence of B_{strain} on the Bragg angle θ. The results, compared with the crystallite size $\langle D \rangle$ measured from scanning electron microscopy (SEM) are reported in Table 2. Note the size deduced from the SEM experiments is an average length of a line parallel to the diffracting plane, passing through the 3-dimensional powder grains. It is then different in essence from the average size $\langle L \rangle$ deduced from the Scherrer's law. Assuming spherical particles, the relation is $\langle D \rangle/\langle L \rangle = 4/3$. After table 2, $\langle D \rangle/\langle L \rangle$ is not the same for both (111) and (222) lines, which is not a surprise since the particles are not perfectly spherical. More important is the fact that $\langle D \rangle/\langle L \rangle$ is in the range $[1, 4/3]$, so that the crystallites probed by XRD have about the same size as the grains probed by SEM. This length measured on the SEM images present a Gaussian-like distribution, with a standard deviation $\sigma = 5\%$. This is an evidence that the grains are the crystallites, so that this size is a test of the crystallinity of the samples. With this regard, the crystallinity of $LiMn_2O_4$ is better for the sample sintered at 800 $^\circ$C than the sample sintered at 750 $^\circ$C.

3.2 Characterization by transport properties

$LiMn_2O_4$ presents a first order Verwey transition at temperature $T_v \simeq 290K$ with an hysteresis of 10 K [5, 15]. Above T_v, the material adopts the normal spinel-type structure (cubic, $Fd3m$) with the octahedral sites occupied by Mn ions in the mixed valence state 3.5. At T_v the lattice undergoes a transition to a very complex orthorhombic phase with incomplete charge ordering [16, 17] of Mn^{3+} and Mn^{4+} ions. The Verwey transition can be evidenced by different experimental techniques. The structural transition associated to the cooperative Jahn-Teller distortion is best studied by neutron experiments [16, 17], while the partial charge ordering related to it can be evidenced by a jump of the electric resistivity $\rho(T)$ at T_v. The existence of this jump can be used as a sensitive test for the crystallinity of the samples, because the Verwey transition is known to be destroyed by structural defects. The resistivity curves of the two $LiMn_2O_4$ samples are reported in Fig. (3). The jump of resistivity at T_v is clearly evidenced in the sample sintered at 800 $^\circ$C, but is barely detectable in the sample sintered at 750 $^\circ$C. We then conclude that the crystallinity is better in the sample sintered at the higher temperature, which is consistent with this conclusion we had drawn from the XRD analysis.

3.3 Characterization by Raman spectroscopy

The Raman spectroscopic studies of lithium manganates with spinel structure, including $Li_{1+x}Mn_{2-x}O_4$ in the spectral range 100-800 cm^{-1} have been investigated in a prior work [18]. The Raman spectra for our x=0 samples is not reported here, since it does not differ from the spectrum published on another sample (see Fig. 2 in [19]) of the same composition, although the mode of preparation was different. Instead, we have reported in Fig. (4) the Raman spectrum for the $x = 0.30$ sample sintered at 750 $^\circ$C, as an illustration of the Raman spectrum of the $x \neq 0$ samples.

Six Raman bands are observed in $LiMn_2O_4$. The low frequency mode at $\simeq$ 300 cm^{-1}, labeled LF-mode in Fig. (4), is an unexpected mode always observed in this material, which could be Raman active due to the cationic disorder that induced a breakdown of the translation symmetry [19]. This mode is tentatively related to the stretching mode of Li in octahedral coordination [20]. The five other modes correspond to the allowed Raman-active modes which can be labeled by their symmetry under O_h^7 spectroscopic group according to the irreducible representation $A_{1g} \bigoplus E_g \bigoplus 3F_{2g}$. The assignment of these modes to the corresponding peaks in the Raman spectra has been made earlier in $LiMn_2O_4$ both experimentally [21] or theoretically by lattice dynamics calculations [22] and force constant model [23]. We can follow up these Raman lines as a function of x, since they are only slightly shifted towards larger wavenumbers as x increases. They are labelled in Fig. (4) according to their symmetry. In particular, a Raman band located at about 625 cm^{-1} in $LiMn_2O_4$, shifted to 634 cm^{-1} in the x=0.3 sample in Fig. (4) is the A_{1g} symmetric Mn-O stretching vibration of MnO_6 groups.

Only these six Raman lines can be seen on the Raman spectra of the samples for compositions in the range $0 \leq x < 0.15$. However, at $x = 0.15$ and at higher Li concentration, an additional line at higher frequency can be detected, with an intensity which increases with x. This external mode is illustrated for $x = 0.3$ in Fig.(4). The range of Li-concentrations where this Raman line can be observed is also the range where the Li_2MnO_3 impurity phase has been detected in our samples. This result suggest a correlation between the two events, with the attribution of this Raman line to a vibration of a molecular edifice of the impurity phase, namely the Mn^{4+}-O stretching vibration of Li_2MnO_3, since Mn is tetravalent in this compound. To investigate the validity of such an assignment, we have studied the x-dependence of the position of this mode. The result, reported in Fig. (5), shows that the wavenumber of this mode shifts from 646 to 656 cm^{-1}, as x increases from 0.15 to 1/3 in $Li_{1+x}Mn_{2-x}O_4$. However, we know from the XRD analysis in section 3.1, that there is no chemical pressure nor strain induced by the host on the Li_2MnO_3 particles, so that the A_{1g} Mn^{4+}-O stretching vibration of the impurity phase should be essentially independent on x, and roughly unchanged with respect to bulk Li_2MnO_3, that is 612 cm^{-1} [24]. Instead, Fig. (5) shows that the additional Raman mode is at higher frequency, and shifts roughly in parallel with the A_{1g} intrinsic mode in the whole composition range $x > 0.15$. This feature opposes the attribution of the additional Raman line to a vibration mode of the impurity phase. Instead, it must be related to the emergence of additional infrared bands in the Fourier transform infrared (FTIR) spectrum of $Li_{1.33}Mn_{1.67}O_4$ attributed to the presence of Li ions in the 16d octahedral sites [18]. As x increases, more and more octahedral sites are occupied by two cations with different masses and charges, and the group-factor analysis of the spinel structure in that case gives two additional infrared components. The breaking of the translational symmetry by the Li-substitution implies that this infrared mode can also be observed in the Raman spectrum, and indeed, the position of the additional Raman mode for $x = 1/3$ in Fig. (5) is the same as that of the FTIR peak reported for this composition in Fig. (7) of ref. [18], namely 665 cm^{-1}. The fact that the additional Raman line is observed only at $x \geq 0.15$ should then mean that, in the range $0 < x < 0.15$ of small Li-substitution, the intensity of this additional Raman line associated to this symmetry-breaking is too small to be detected. The frequency shift of the intrinsic A_{1g} mode and the additional one with x is mainly due to the increase in the mixed valence of the Mn as a function of x in the $Li_{1+x}Mn_{2-x}O_4$ phase.

Note the Raman efficiency of $LiMn_2O_4$ is weakened by the electrons, as this material is a small-polaron semiconductor in which the electron conductivity arises from hopping between the two oxidation states of manganese ions [25]. This electronic property is also responsible for a baseline which is not flat, and can be represented by a very broad peak illustrated in Fig. (4). The tailing structure around 200 cm^{-1} is due to the Rayleigh scattering. In the fitting procedure, this tailing structure is assumed to be of the Lorentzian form and is added to the baseline. Note it is always possible to fit such a tailing structure in such a small range of wavenumbers 200 - 250 cm^{-1} by a Lorentzian function, as only this 'wing' of the Rayleigh peak is detected in our experiments. Therefore the choice of the Lorentzian shape should be simply considered as a simple way to get rid of this contribution in the spectrum of Fig. (4), without any physical meaning that would imply extrapolation of this law to the unexplored region of smaller wavenumbers.

4 Magnetic properties

4.1 $LiMn_2O_4$ ($x = 0$)

The temperature dependence of the magnetization M of the $LiMn_2O_4$ samples measured under an applied field $H = 10$ kOe are reported in Fig (6) under the form of $H/M(T)$. The main difference is an anomaly in the temperature range 40-50 K for the sample sintered at 800 ° C. The magnetization curves on this sample, illustrated in Fig. (7) show that this anomaly corresponds to the onset of an extrinsic magnetic component which saturates very fast with the magnetic field, superposed to the paramagnetic intrinsic component. This is the signature of ferrimagnetic Mn_3O_4 impurity phase, identified by its spin ordering temperature at 42 K [26] . The comparison at $T = 4.2$ K between the low field magnetization in our sample and the magnetization of Mn_3O_4 [27] allows us to deduce the amount of this impurity phase in the sample, namely 0.5%. This is below the detection threshold of the X-ray diffraction analysis, which explains that it could not be detected by XRD. On another hand, this impurity phase does not exist in the sample sintered at 750 ° C. Therefore, both sintering temperatures have an advantage and a disadvantage: sintering at 750 ° C avoids the formation of Mn_3O_4 impurity phase, but the crystallinity of the host $LiMn_2O_4$ matrix is not as good as in the case of a sintering at 800 ° C.

Both $LiMn_2O_4$ samples show an anomaly at low temperature $T \simeq 15$ K where the zero-field-cooled magnetic susceptibility goes through a maximum. The large difference between field-cooled and zero-field-cooled data, best evidenced on the sample sintered at 750 $^\circ$C, is very similar to the standard behavior of spin glasses. Actually, a spin glass ordering for this material has been proposed by several authors [28, 29]. However, data in Fig. (6) have been recorded in a very large magnetic field $H = 10$ kOe, while any spin glass behavior is known to be destroyed under applied field one order of magnitude smaller. Therefore, the spin freezing evidenced in our sample below 15 K cannot be the onset of a spin glass phase. Instead, it could be the onset of some antiferromagnetic domains of finite size. This behavior is consistent with the coexistence of antiferromagnetic Bragg peaks with the magnetic diffuse peak in the range 10-65 K observed in the neutron spectra of some $LiMn_2O_4$ samples [30]. On another hand, no long range antiferromagnetic ordering takes place in our samples. Such an ordering has been observed in one prior work, at a Néel temperature $T_N = 65$ K [31]. The antiferromagnetic ordering might also be a criterion for the crystallinity of the sample too. Indeed, an antiferromagnetic ordering should be associated to the onset of a complete charge ordering, and then also to a transition to an insulating phase, just like in Fe_3O_4 where a jump in resistivity by two orders of magnitude has been observed. To our knowledge, the resistivity curves of $LiMn_2O_4$ reported in the literature do not show an anomalous behavior on the resistivity curves at 65 K (nor actually at any temperature except at T_v) but they have only been reported in those samples which do have a Néel temperature. The complete spin and charge ordering might then be a criterion for crystallinity more stringent than the simple observation of the Verwey transition at T_v. In this context, our sample sintered at 800 $^\circ$C is an intermediate between two categories of samples. Samples of poorer crystallinity are characterized by the lack of any spin freezing [32, 34, 35], with only the antiferromagnetic diffusive peak in the neutron spectra [36]. Samples of better crystallinity show long range antiferromagnetic ordering evidenced by both the magnetic susceptibility data and the existence of Bragg neutron diffraction peaks [31].

The Curie-Weiss law is approximately satisfied in the range 200-300 K, from which we can find the paramagnetic temperature $\theta = -260$ K for the sample $LiMn_2O_4$ sintered at 800 $^\circ$C. This value is in quantitative agreement with former results [37]. On another hand, it is markedly different from the value $\theta = -296$ K we found for the sample sintered at 750 $^\circ$C, close to the value $\theta = -315$ K reported in another work [32]. This huge variation from one sample to another is quite unusual, and is again a specificity of $LiMn_2O_4$. The explanation comes from different factors. First we note that $\mid \theta \mid$ is of the same order of magnitude as room temperature. However, the Curie-Weiss law is a mean field law which is justified only in the limit where spin correlations are negligible. Such correlations are negligible only at temperatures typically $T > 2\theta$. Therefore, the analysis of the magnetic properties at $T < T_v$ is not justified, although it is systematically done and never discussed in all the prior works. The importance of such short range spin correlations can be evidenced by a small upward curvature of the inverse magnetic susceptibility. The difference in the values of θ among samples, when forcing the fit of the susceptibility curve by the Curie-Weiss law, is then attributable to a sensitivity of the local spin correlations to the conditions under which the samples have been prepared. This is consistent with the extreme dependence of the physical properties of these samples to the mode of preparation. Note however that we cannot find any relation between θ and charge ordering. In particular, the value $\mid \theta \mid = 315$ K in ref. [32] has been found for a sample which undergoes the Verwey transition with a jump in the resisitivity curve at T_v. This is close to the value we found for our sample in which the transition is smeared out, while our sample which presents such a transition has a much lower $\mid \theta \mid$. This lack of correlation suggests that θ and the Verwey transition are a probe of the crystallinity at two different scales. The lack of partial charge ordering and long-range magnetic ordering results from disorder effects at a mesoscopic scale, the deviation from a Curie law, which affects the experimental value of θ is due to short-range spin fluctuations, i.e. at a local scale.

The substitution of Mn by Li at the octahedral site has been explored already by [32] for $x \leq 0.065$. The main effect of this substitution at such small values of x is the destruction of the Verwey transition. This is consistent with the strong sensitivity of charge ordering with the structural defects, already discussed. Since the Verwey transition cannot be observed in this case, we have chosen to prepare all the $Li_{1+x}Mn_{2-x}O_4$ samples in this work using a sintering temperature 750 ° C, to minimize the pollution of the sample (and their magnetic properties) by Mn_3O_4. Since the samples investigated for $x \neq 0$ are in the range $0.05 \leq x \leq 0.33$, the present work can be considered as an extension of this prior work in [32].

4.2 $\mathbf{Li_{1+x}Mn_{2-x}O_4}$ $(0 < x \leq 0.33)$

The susceptibility curves of $Li_{1+x}Mn_{2-x}O_4$ series are illustrated in Fig. (8). As x increases, $\mid \theta \mid$ decreases, so that the antiferromagnetic spin correlations decrease. It also means that the analysis of the magnetic susceptibility is now justified. The smaller values of $\mid \theta \mid$ and the correlated fact that $H/M(T)$ curves are also linear down to lower temperature now fully validates the analysis of the magnetic susceptibility according to the Curie-Weiss law. If we assume that only the manganese ions contribute efficiently to the magnetization, the Curie constant C can be written:

$$C = \frac{N_A p_{\text{eff}}^2 \mu_B^2}{3k_B}, \tag{1}$$

with N_A the Avogadro number (since we have expressed the magnetization per mole unit in this work), μ_B is the Bohr magneton, and p_{eff} the effective moment (in μ_B unit) associated to the (2-x) Mn ions in the chemical formula. Assuming that Mn^{3+} and Mn^{4+} in proportion y and $(1-y)$ respectively, carry an effective moment $\mu(Mn^{3+,4+})$ in μ_B unit, we find:

$$p_{\text{eff}}^2 = (2-x)[y\mu(Mn^{3+})^2 + (1-y)\mu(Mn^{4+})^2]. \tag{2}$$

y is determined by the equation of neutrality of the electronic charge :

$$y = \frac{1-3x}{2-x}. \tag{3}$$

The two Curie-Weiss parameters θ, p_{eff} and their dependence on x are reported in Figs. (9, 10). For the samples $x > 0.2$ which contain Li_2MnO_3, the contribution of this impurity phase has been subtracted first. For this purpose, the magnetic susceptibility of a Li_2MnO_3 has been measured (not shown here), and has been weighted by the ratio $[Li_{1+x}Mn_{2-x}O_4]/[Li_2MnO_3]$ determined from X-ray analysis for each sample. The resulting signal has been subtracted from the rough data measured for the $Li_{1+x}Mn_{2-x}O_4$ samples to extract the intrinsic component. For the samples with the highest concentration in Li_2MnO_3, this correction was found non negligible, lowering p_{eff} by about 0.2.

5 Electrochemical properties

Charge-discharge profiles were obtained for all the compounds at current density 0.25 mA/cm^2 (C/10 rate). Figures 11, 12 show the typical voltage profiles of the $Li_{1+x}Mn_{2-x}O_4$/$LiPF_6$-EC-DEC/Li cells at 25 $^\circ$C for different molar ratios of Li to Mn. The compound $Li_1Mn_2O_4$ displays a voltage profile of a spinel cathode with the characteristic two-step reaction at 3.95 and 4.10 V [38], and delivers an initial capacity of 108.7 mAh/g. The initial capacity decreases upon increasing the molar ratio of Li to Mn, due to the increase of the electrochemically inactive Mn^{4+} ions in the $Li_{1+x}Mn_{2-x}O_4$ spinel lattice. It is easily observed that the decreasing capacity is associated with the disappearance of the first voltage plateau. Finally, a capacity 70.8 mAh/g is obtained for the Li-rich compound (x=0.20) in which the average oxidation state of manganese is 3.77. Moreover, the end-member compound with $x = 0.33$ is a non active material for a 4-volt electrode, as expected since all the Mn ions are in the Mn^{4+} ionization state in that case.

6 Analysis

According to Fig. (9), $\mid \theta \mid$ decreases almost linearly with x at small x and then vanishes at $x = 0.3$. In prior works where data were available at small x, i.e. in the quasi-linear regime of $\theta(x)$, a simple extrapolation at larger x suggested that the decrease of $\mid \theta \mid$ when x increases was related to an increase in ferromagnetic interactions at the expense of antiferromagnetic ones [32]. Indeed, looking at the superexchange interactions associated to the bonding at 90°, the Mn^{4+} -O- Mn^{4+} interaction is ferromagnetic, while the Mn^{4+} -O- Mn^{3+} and Mn^{3+} -O- Mn^{3+} ones are antiferromagnetic according to the Goodenough-Kanamori rules [33]. The increase in the concentration of Mn^{4+} upon x was then expected to increase the density of ferromagnetic interactions at the expense of the antiferromagnetic ones if only these superexchange interactions between Mn nearest neighbors via oxygen at 90° are taken into account. However, the fact that θ does not vary linearly with x at larger x, and saturates at $\theta = 0$ instead of changing sign, opposes this former analysis. In particular, an increase in the ferromagnetic interactions would result in the onset of ferrimagnetism which is clearly not observed. Instead, the increase in x results in a dilution of the antiferromagnetic interactions. The reluctance of the material to undergo a transition to long-range magnetic order is then attributable to the *geometrical* frustration of Mn magnetic moments on the B sites of the spinel lattice. Similar geometrical frustration effects inherent to this topology of the spinel lattice on the magnetic properties with nearest neighbor antiferromagnetic interactions only have been also observed in other materials with Fe as magnetic ions instead of Mn [39]. This is quite consistent with the fact that the long range (antiferromagnetic) magnetic ordering in $Li_{1+x}Mn_{2-x}O_4$ takes place only in samples which have undergone a Verwey transition, i.e. in these samples which have crystallized (below T_v) in a lattice with a different geometrical arrangement of lower symmetry, owing to the cooperative Jahn-Teller distortion. Actually, if we consider the sample with $x = 1/3$ in which only the Mn ions are in the Mn^{4+} valence state, we find $\theta \simeq 0$ which can be considered as the direct evidence that the ferromagnetic Mn^{4+}-O-Mn^{4+} interactions are totally negligible in this material, and thus do not play any significant role. In particular, the ferromagnetic component reported in $M(H)$ at low temperature on the $x = 0.003$ and $x = 0.065$ samples in ref. [32] is not related to the Mn^{4+} -O- Mn^{4+} interaction, as it was suggested in this work at a time where the influence of the sintering temperature and mode of preparation of the samples on the impurity phases has not been realized. Instead, it is an extrinsic property most likely due to the presence of Mn_3O_4 clusters in the matrix, like in our own sample $x = 0$ sintered at 800 ° C.

According to Eq. (3), the increase of x means a decrease of the proportion y of Mn^{3+} in the matrix. The fact that the Mn^{4+}-O-Mn^{4+} magnetic interactions are negligible suggests that the increase in x only results in the dilution of the antiferromagnetic short range interactions associated to Mn^{3+} on a geometrically frustrated lattice. In such a case, we expect that $\theta \simeq 0$ for $x > x_c$ with x_c the value of x corresponding to the situation where the Mn^{3+} concentration $(2 - x)y$ reaches the percolation threshold. As the percolation threshold for the Mn sublattice is 0.16, Eq. (3) shows that this situation is reached at $1 - 3x_c = 0.16$, namely $x_c = 0.28$, in good agreement with the experimental results displayed in Fig. (9). On another hand, in case all magnetic correlations would exist in Mn^{4+}-O-Mn^{4+}, Mn^{3+}-O-Mn^{4+}, Mn^{3+}-O-Mn^{3+} paths, the dilution effect associated to the Li-substitution would imply that θ goes to zero when the total Mn concentration $2 - x$ would reach the critical value 0.16, namely an unphysical result $x_c = 1.84$. The vanishing of θ close to $x_c = 0.28$ in Fig. (9) is then also the evidence that only the antiferromagnetic Mn^{3+}-Mn^{3+} interactions mediated via oxygen ions are responsible for the magnetic properties. The present work is then in quantitative agreement with the dependence of θ with x, which was deduced from the analysis of the integrated intensity of the EPR line associated to the $Li_{1+x}Mn_{2-x}O_4$. The contradiction between magnetic and EPR results outlined in [10] just came form a positive value $\theta = +40$ K in $Li_4Mn_5O_{12}$ deduced from magnetic measurements [40]. Actually, there is no contradiction but quantitative agreement between EPR analysis in [10] and our direct magnetic measurements reported here. Indeed, extrapolation of these results to $Li_4Mn_5O_{12}$ would predict $\theta \simeq 0$ for this material. We then suspect that the larger value of θ reported in [40] comes from some extrinsic effect in the particular sample which had been measured. This is supported by the fact that the authors themselves outlined the large sample-dependence of the value of θ in this material, since they found $\theta \simeq +2$ K in another $Li_4Mn_5O_{12}$ sample [40].

The theoretical effective moment carried by Mn^{4+} (spin $S = 3/2$) is $\mu(Mn^{4+}) = 3.87\ \mu_B$. That of Mn^{3+} depends on the strength of the crystal field. In high spin complexes it is 4.90 μ_B, in low spin complexes it is 2.83 μ_B. The theoretical value of p_{eff} as a function of x are also reported in Fig. (10) together with experimental data for comparison, for both the low and high spin configurations of Mn^{3+}. Since the low spin state would lead to an increase of p_{eff} with x, while the experimental value is decreasing monotonously with x in the whole range of concentrations x we have explored, we can conclude that the Mn^{3+} remains in the high spin configuration at all concentrations x. On another hand, the theoretical value is systematically larger than the experimental one. This is the case, in particular, for $x = 1/3$ where only Mn^{4+} are present so that the magnetization of this ion is below theoretical. This is consistent with the observation of an effective magnetic moment below theoretical observed as a function of the average oxidation state of manganese for lithium magnetospinels in the $LiMn_2O_4$-$Li_2Mn_4O_9$-$Li_4Mn_5O_{12}$ [40]. The experimental value of the magnetic moment of Mn^{4+} as deduced from the data at $x = 1/3$ is $\mu(Mn^{4+}) = 3.11\ \mu_B$ instead of the value 3.87 μ_B predicted for this ion in an octahedral field (note that p_{eff} differs from $\mu(Mn^{4+})$ by a factor $\sqrt{2}$ due to the factor $(2 - x)$ entering our definition of p_{eff}). We then have reported the full line in Fig. (10) that is the theoretical function p_{eff} as a function of x, assuming $\mu(Mn^{4+}) = 3.11\ \mu_B$ and $\mu(Mn^{3+}) = 4.90\ \mu_B$. The result is found in reasonable agreement with the experiments, which shows that the effective moment carried by Mn^{3+} is in agreement with the value 4.90 μ_B predicted for this ion in the high spin state. The rather low moment observed in the samples is then primarily due to a value of the magnetic moment carried by Mn^{4+} ions which is found to be significantly smaller than expected for a spin $S = 3/2$. This lower value suggests a strong crystal field effects on the sites occupied by these ions that may give rise to an unexpected magnetic anisotropy originating from these ions.

The lowering of the magnetic moment carried by Mn^{4+} ions is another evidence that the material is not purely ionic, and the bond between Mn^{4+} and its neighbors is partly covalent. Such a covalent effect has been investigated in other manganese compound including MnSb [41]. In this compound, Mn is essentially in the divalent Mn^{2+} configuration, since the charge transfer of Mn to Sb is very small in the paramagnetic phase. Nevertheless, the magnetic moment carried by Mn^{2+} ions is reduced to 3.24 μ_B instead of 5 μ_B, as a result of a small covalent bonding that leads to just a very small charge transfer between Mn and Sb (the reason why the magnetic moments remain localized on the manganese ions), but leads to a spin depolarization of the d-states that reduce the localized magnetic moment. Such a behavior is also met in other materials involving transition metal elements (and not only manganese) such as the Heusler alloys [42]. We are in the same situation here, although the reduction of the magnetic moment is smaller. Note the non-vanishing covalent mixing between the $3d$ states of the Mn^{4+} ions and the electronic states of neighboring atoms also explains the presence of electrons previously detected by transport experiments and affecting the baseline of the Raman spectra of our samples (see section 3.3). Note the value of the effective moment in the $x = 1/3$ sample is sufficient to determine unambiguously the effective magnetic moment of Mn^{4+}, since all the manganese ions are in this ionization sate in that case. The agreement beween the dot/broken curve and the experiments in Fig. (10) at any other Li-concentration is thus the experimental evidence that the reduction of the magnetic moment is entirely located on the Mn^{4+} ion and not on the Mn^{3+} ions. This is due of the relative energies of the different ionic states of the manganese ions. Since these energies are the result of exchange plus Coulomb correlations of the multi-electron system in the d-shell, the quantitative estimate in the present case would require a calculation of the electronic structure of our compound within the DFT+U method that is appropriate for these highly correlated electron systems. The concept is to treat the localized d-states by the Hubbard Hamiltonian (correlation potential U) while retaining the Hamiltonian in a density functional theory (DFT) for the other more delocalized states. Such a calculation that has been done successfully on few highly correlated systems (including MnSb compound above mentioned) does not exist yet on $LiMn_2O_4$ and is beyond the scope of this paper. However, we can qualitatively explain why the covalent effect is on the Mn^{4+} ions as follows. The most stable electronic state of manganese is the divalent state Mn^{2+}, since it realizes the configuration of half-filled d-shell. The larger and larger exchange plus correlation energy of the d-electrons as the charge on the manganese increases in the sequence $2+ \rightarrow 3+ \rightarrow 4+$ favors the covalent effect that amounts to a charge transfer reducing the positive electrostatic charge on the d-shell of the manganese. This effect is naturally much larger for Mn^4+ than for Mn^3+ since the departure of the electrostatic charge from the divalent state is twice larger for the Mn^{4+} configuration.

These results provide us with some enlightenment on EPR data published so far on this material. In Li-rich samples ($x > 0$), two main lines have been observed. A broad line attributed to the $Li_{1+x}Mn_{2-x}O_4$ spinel phase, and a sharp line attributed to the Li_2MnO_3 phase [7]. Since the sharp line is not observed in $LiMn_2O_4$ [7] and since its existence in $x \neq 0$ depends on the sintering temperature [9], its attribution to this impurity phase is justified. The fact that this line has been observed when Li_2MnO_3 impurity phase is not evidenced by XRD analysis should then attributed to the fact that EPR experiments are much more sensitive to the existence of this phase. As a result, the existence of this line in the EPR spectra in [10] should be considered as an indication that the Li_2MnO_3 impurity phase is only the order of the %, i.e. below the threshold of detection by XRD analysis rather than questioning on the origin of this EPR line. On another hand, the ESR spectra of $LiMn_2O_4$ in [9] show at low temperature an additional structure made of 6 hyperfine lines with nearly equal splitting, which appear as the sample is heated from 3.5 to 80 K. This feature has been attributed at that time to Mn^{4+} ions. Such an interpretation, however, is made difficult by the fact that the two sharp discontinuities associated to the $| +1/2\rangle \longleftrightarrow | -1/2\rangle$ transitions are not observed in the spectra. The reason invoked is that the Mn^{4+} ions are not impurities, so that fluctuations of the magnetic interactions and crystal field effects from site to site should broaden the spectrum. But actually, such effects are expected to broaden the ESR spectrum to the point where no hyperfine structure can be detected, so that the spectrum associated to Mn^{4+} should be a single broad line, and this is what is observed. Another hypothesis is that this line structure is the spectrum characteristics of Mn^{2+} impurities in such a small concentration that the hyperfine structure can be seen [43]. Such Mn^{2+} in concentration lower than 1% can be found in the Mn_3O_4 impurity phase we have detected by magnetic measurements on the $LiMn_2O_4$ sample sintered at 800 °C in the present work. The fact that the linewidth of this hyperfine structure does not depend on x [9] also suggests a lack of coupling with the $Li_{1+x}Mn_{2-x}O_4$ spinel phase, i.e. Mn^{2+} ions in an impurity phase. We are thus led to suggest that the 6-lines structure of the EPR spectrum evidenced in some samples [9] is attributable to this impurity phase. Additional proof is provided by the fact that this hyperfine structure is not observed at low temperature (i.e. in the temperature range where Mn_3O_4 is ferromagnetic); it can be observed only at (or above) 40 K, while the Curie temperature of Mn_3O_4 is 42 K. Finally, another proof is provided by the comparison with the EPR spectra obtained on samples which have been prepared by following the wet chemical route, and sintered at 700 °C [10]. No such 6-line structure has been detected in the EPR spectra for such materials. This is consistent with the results of the present work that show lowering the sintering temperature from 800 °C to 750 °C is sufficient to get rid of the Mn_3O_4 impurity phase.

7 Conclusion

$Li_{1+x}Mn_{2-x}O_4$ magnetic and transport properties are strongly dependent on the structural properties. The magnetic measurements allowed us to detect Mn_3O_4 impurity phase in concentration (0.5 %) too small to be detected by X-ray analysis, in sample sintered at 800 °C. This impurity phase is cured by decreasing the sintering temperature at 750 °C. On another hand, Li_2MnO_3 impurity phase is observed at $x \geq 0.15$ in concentration which increases with x. The wet-chemical route did not allow us to get rid of this impurity phase, although its concentration is significantly reduces with respect to other preparation techniques. The impurity phases, when they exist, are not expected to alter the intrinsic properties of $Li_{1+x}Mn_{2-x}O_4$. At least for $x = 0$, the proof is provided by the fact that the Verwey transition and the long-range antiferromagnetic measurements have been reported in a recent past on a sample which also contains Mn_3O_4 as an impurity phase [31]. On another hand the sintering temperature also affects the intrinsic properties. In particular, the degree of charge ordering is very much dependent on the structural properties, and the sample preparation. The x-dependence of the magnetic properties show that these properties are dominated by the geometrical frustration of the antiferromagnetic interactions inherent to the spinel lattice, while the ferromagnetic interactions associated to Mn^{4+}-Mn^{4+} bonding at 90 ° are negligible in this material. This frustration is in essence the reason why the samples do not undergo a transition to a long-range magnetic ordering despite the strongly antiferromagnetic interactions, except at $x = 0$ in those of the samples presumably with the highest crystallinity. The Mn^{4+} ions that are electrochemically inactive also carry a small effective moment that we can attribute to covalent effects evidenced otherwise by transport and optical properties, and may be also linked to the fact that the Mn^{4+}-Mn^{4+} magnetic interactions above mentioned are negligible. The separation between intrinsic an extrinsic effects allowed us to achieve an overall understanding of the various physical properties (magnetic properties, optical properties, EPR spectra) of this material.

References

[1] M. M. Tackeray, W.I.F. David, P.G. Bruce, J.B. Goodenough, Mater. Res. Bull. **18**, 461 (1983).

[2] J. B. Goodenough, M. M. Tackeray, W.I.F. David, P.G. Bruce, ReV. Chim. Miner. **21**, 435 (1984).

[3] T. Ohzuku, M. Tikagawa, T. Hirai, J. Electrochem. Soc. **137**, 769 (1990).

[4] J. M. Tarascon, W. R. McKinnon, F. Coowar, T. N. Bowmer, G. Amatucci, and D. Guyomard, J. Electrochem. Soc. **141**, 1421 (1994).

[5] A. Yamada, J. Solid State Chem. **122**, 160 (1996).

[6] V. Massarotti,, M. Bini, , and D. Capsoni, Z. Naturforsch. A**51**, 267 (1996).

[7] V. Massarrotti, D. Capsoni, D. Bini, C. B. Azzoni, and A. Paleari, J. Solid Stat. Chem. **128**, 80 (1997).

[8] V. Massarrotti, D. Capsoni, D. Bini, G. Chiodelli, C. B. Azzoni, M. C. Mozzati, A. Paleari, J. Solid Stat. Chem. **147**, 509 (1999).

[9] F. Gendron, C. Julien, in *Materials for Lithium-ion Batteries*, eds. C. Julien and Z. Stoynov, Kluwer Academic Publ., Dordrecht 2000, p 543.

[10] J. R. Dygas, M. Kopc, F. Krok, F. Gendron, and C. M. Julien, Electrochem. Soc. Proc. **11**, 63 (2005).

[11] C.M. Julien, Solid State Ionics **177**, 11 (2006).

[12] P. Mustarelli, V. Massarotti, M. Bini, and D. Capsoni, Phys. Rev. B **55**, 12018 (1997).

[13] S.R.S. Prabaharan, S.S. Michael, C. Julien, J. Inorganic Mat. **1**, 21 (1999).

[14] K. Levenberg, Quart. Appl. Math. **2**, 164, 1944; D. Marquardt, SIAM J. Appl. Math. **11**, 431, 1963

[15] A. Yamada and M. Takena, Mater. Res. Bull. **30**, 715 (1995).

[16] J. Rodriguez-Carvajal, G. Rousse, C. Masquelier, and M. Hervieu, Phys. Rev. Lett. **81**, 4660 (1998).

[17] M. Takahashi and K.-I. Ohshima, J. Cryst. Soc. Jpn. **48**, 17-24 (2006).

[18] C. M. Julien, Solid Stat. Ionics **177**, 11 (2006).

[19] C. M. Julien and M. Massot, J. Phys.: Condens. Matter **15**, 3151 (2003).

[20] C. Julien, C. Letranchant, M. Lemal, S. Ziokiewicz, S. Castro-Garcia, J. Mater. Sci. **37**, 2367 (2002).

[21] C. M. Julien, A. Rougier, E. Haro-Poniatowski and G. Nazri, Mol. Crys. Liq. Crys. **311**, 81 (1998).

[22] B. Ammundsen, G.R. Burns, M.S. Islam, H. Kanoh, and J. Rozière, J. Phys. Chem B **103**, 5175 (1999).

[23] M.M. Sinha and H.C. Gupta, Physica B **316/317**, 166 (2002).

[24] C. M. Julien and M. Massot, Mater. Science. Engin. B **100**, 69 (2003).

[25] J. B. Goodenough, A. Manthiram, and B. Wnetrzewski, J. Power Sources **43/44**, 269 (1993).

[26] K. Dwight and N. Menyuk, Phys. Rev. **119**, 1470 (1960).

[27] O. V. Nielsen, and L. W. Roeland, J. Phys. C: Solid State Phys. **9**, 1307 (1976).

[28] P. Endres, B. Fuchs, S. Kemmler-Sack, K. Brandt, G. Faust-Becker, and H. -W. Praas, Solid State Ionics **89**, 221 (1996).

[29] Y. Jang, F. C. Chou, and Y. Chiang, Appl. Phys. Lett. **74**, 2504 (1996).

[30] A. S. Wills, N. P. Raju, and J. E. Greedan, Chem. mater. **11**, 1510 (1999).

[31] I. Tomeno, Y. Kasuya and Y. Tsunoda, Phys. Rev. B **64**, 094422 (2001).

[32] Y. Shimakawa, T. Numata, and J. Tabuchi, J. Solid State Chem. **131**, 138 (1997).

[33] B. Goodenough, Magnetism and the Chemical Bond (Wiley, New York, 1963).

[34] G. Blasse, J. Phys. Chem. Solids **27**, 383 (1966).

[35] C. B. Azzoni, M. C. Mozzati, A. Paleari, D. Capsoni, and M. Bini, Z. Naturforsch. A **53**, 693 (1998).

[36] Y. Oohra, J. Sugiyama, and M. Kontani, J. Phys. Soc. Jpn. **68**, 242 (1999).

[37] C. M. Julien, A. Ait-Salah, A. Mauger, and F. Gendron in *Portable and emergency energy sources*, ed. by Z. Stoynov and D. Vladikova, Marin Dynov Publishing House, Sofia 2006, p 71.

[38] M.M. Thackeray, Prog. Solid State Chem. **25**, 1 (1997).

[39] M. Ostorero, A. Mauger, M. Guillot, and M. Escorne, Phys. Rev. B **40**, 391 (1989).

[40] C. Masquelier, M. Tabuchi, K. Ado, R. Kanno, Y. Kobayasi, Y. Maki, O. Nakamura, J. B. Goodenough, J. Solid State Chem. **123**, 255 (1996).

[41] R. Coehoorn and C. Haas, Phys. Rev. B **31**, 1980 (1985) and references therein.

[42] J. Kübler, A. R. Williams, and C. B. Sommers, Phys. Rev. B**28**, 1745 (1983).

[43] J. S. van Wieringen, Discussions of the Faraday Society **19**, 118 (1955).

Figure 1: X-ray diffraction pattern of $Li_{1+x}Mn_{2-x}O_4$ for two different compositions x. The insert emphasizes the region between the (311) and (400) lines, including the (222) line that has been used to determine the size of the crystallites according to the Scherrer's law. The Miller indices for the $Li_{1+x}Mn_{2-x}O_4$ have been reported (for the $x = 0.33$ sample). The symbol (*) in the insert associated with this spectrum points out two lines associated to the Li_2MnO_3 impurity phase.

Figure 2: Lattice parameter of $Li_{1+x}Mn_{2-x}O_4$ as a function of x deduced form Rietveld refinement of XRD spectra. The square symbol is the experimental result for $LiMn_2O_4$ sintered at 800 ° C. Triangles are experimental points for the samples sintered at 750 ° C. The full line is a guide for the eyes.

Figure 3: Arrhenius plot of the electrical conductivity of the $LiMn_2O_4$ sintered at 800 and 750 °C.

Figure 4: Raman spectrum of $Li_{1+x}Mn_{2-x}O_4$ sample for x=0.30. The thick solid line is the spectrum calculated by fitting the data with decomposition of the spectrum in Raman peaks with Gaussian profile (in addition to the baseline). The decomposition of the spectrum is also reported in the figure. The LF (low frequency)-mode is related to Li vibrations. The five modes at higher energy are labeled according to their symmetry under O_h^7 spectroscopic group. The mode at the highest energy is the external mode associated to the Mn^{4+}-O stretching mode in the Li_2MnO_3 impurity phase (observed only at $x \geq 0.15$).

Figure 5: x-dependence of the A_{1g} Raman peak (full dots) and the external mode (squares). The external mode exists only. at $x \geq 0.15$) in $Li_{1+x}Mn_{2-x}O_4$ samples.

Figure 6: H/M where M is the magnetization measured under applied magnetic field H=10 kOe, for the $LiMn_2O_4$ sintered at 800 and 750 °C. Data have been recorded following zero-field cooled (ZFC) and field-cooled (FC) procedures described in the text.

Figure 7: M(H) of the $LiMn_2O_4$ sintered at 800 °C as a function of the applied magnetic field, for different temperatures.

Figure 8: Same as in Fig.(6) for $x \neq 0$.

Figure 9: Paramagnetic Curie temperature as a function of x in $\mathrm{Li}_{1+x}\mathrm{Mn}_{2-x}\mathrm{O}_4$.

Figure 10: Effective magnetic moment in Bohr magneton unit as a function of x in $Li_{1-x}Mn_{2-x}O_4$.

Figure 11: Voltage profiles of the $Li_{1+x}Mn_{2-x}O_4$/$LiPF_6$-EC-DEC/Li cells at 25 °C for charge/discharge at C/10 rate.

Figure 12: Same as Fig. 11, for two other compositions.

powders	phases	% phase	cell constants (Å)	volume (Å^3)
x=0 (800 ° C)	$LiMn_2O_4$	100	8.2509(2)	571.71(4)
x=0 (750 ° C)	$LiMn_2O_4$	100	8.23716(2)	558.90(4)
x=0.05	$Li_{1.05}Mn_{1.95}O_4$	100	8.22126(2)	555.67(3)
x=0.10	$Li_{1.10}Mn_{1.90}O_4$	100	8.20576(2)	552.53(3)
x=0.15	$Li_{1.15}Mn_{1.85}O_4$	100	8.19304(2)	549.97(3)
x=0.20	$Li_{1.20}Mn_{1.80}O_4$	100	8.18158(2)	547.66(3)
x=0.25	$Li_{1.25}Mn_{1.75}O_4$	90.54	8.17446(2)	546.22(3)
	Li_2MnO_3	9.46	a=4.9047(2) b=8.5406(4) c=5.0264(1), $\beta = 108.72$	199.41(0)
x=0.30	$Li_{1.30}Mn_{1.70}O_4$	88.7	8.16712(2)	544.73(3)
	Li_2MnO_3	11.3	a=4.9293(2) b=8.5050(3) c=5.0322(1), $\beta = 109.05$	199.42(6)
x=0.33	$Li_{1.33}Mn_{1.67}O_4$	87.32	8.16873(2)	545.08(5)
	Li_2MnO_3	12.68	a=4.9327(2) b=8.4989(3) c=5.0240(1), $\beta = 108.87$	199.30(5)

Table 1: Rietveld analysis of the powders investigated in this work. Since the $Li_{1+x}Mn_{2-x}O_4$ is crystallized in the cubic spinel phase, so that the lattice is entirely defined by the lattice parameter $a = b = c$. Only the $LiMn_2O_4$ sample labelled x=0 (800 ° C) has been heated at 800 ° C. For all the other samples, the sintering temperature is 750 ° C.

crystallite	size from XRD (nm)		from SEM (nm)
	(111)	(222)	
x=0 (800 °C)	100.4	139.7	140
x=0 (750 °C)	74.4	84.2	87
$Li_{1.05}Mn_{1.95}O_4$	71.1	80.2	86
$Li_{1.10}Mn_{1.90}O_4$	70.5	62.4	86
$Li_{1.15}Mn_{1.85}O_4$	75.7	66.1	78
$Li_{1.20}Mn_{1.80}O_4$	71.2	58.3	75
$Li_{1.25}Mn_{1.75}O_4$	62.7	45.6	78
$Li_{1.30}Mn_{1.70}O_4$	60.4	42.8	65.5
$Li_{1.33}Mn_{1.67}O_4$	60.0	43.9	70

Table 2: Crystallite size deduced from Rietveld refinement on (111) and (222) XRD lines of $Li_{1+x}Mn_{2-x}O_4$ (same samples as in table 1). For comparison, the grain size measured from SEM is also reported (last column).

Figure1

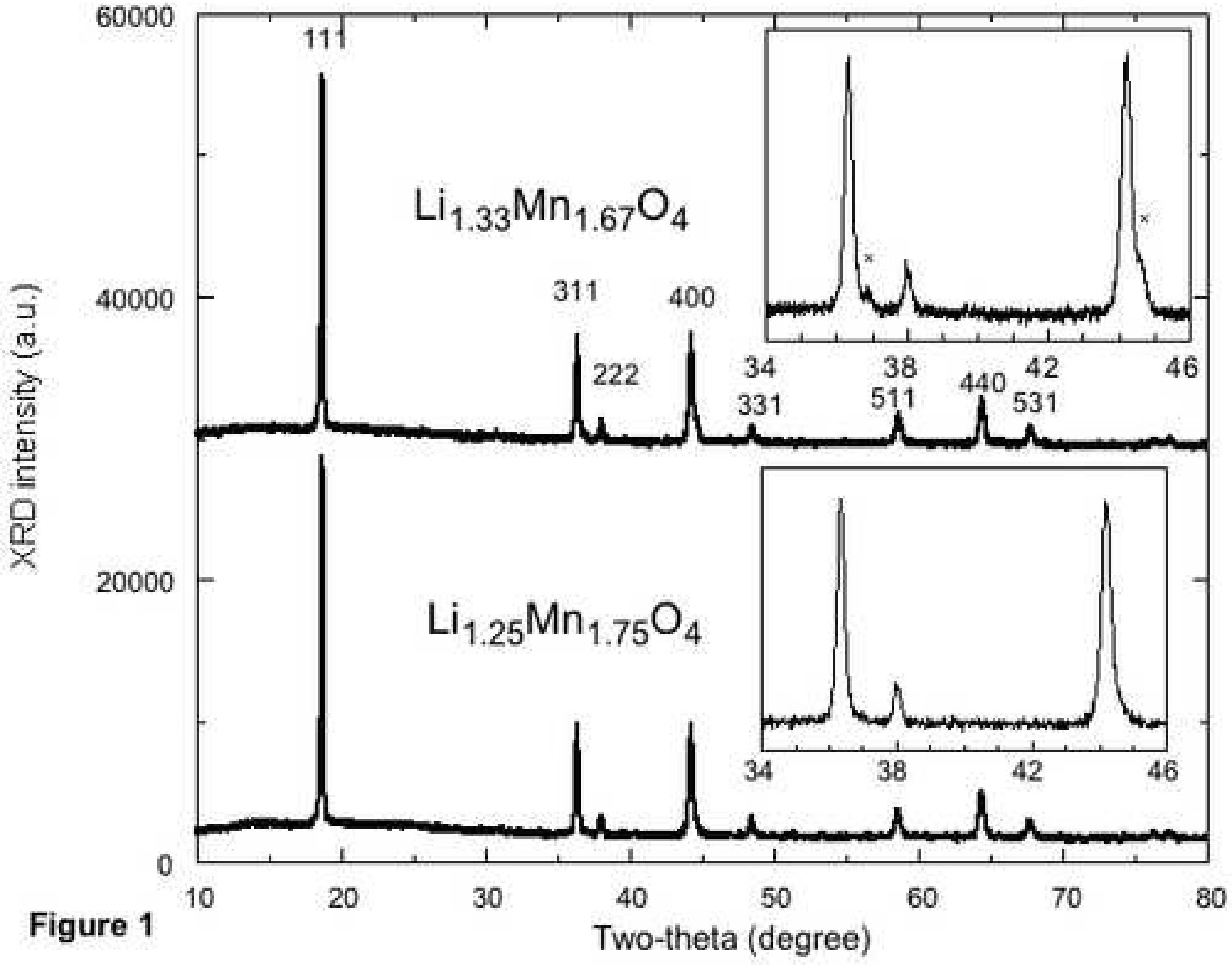

Figure 1

Figure 2

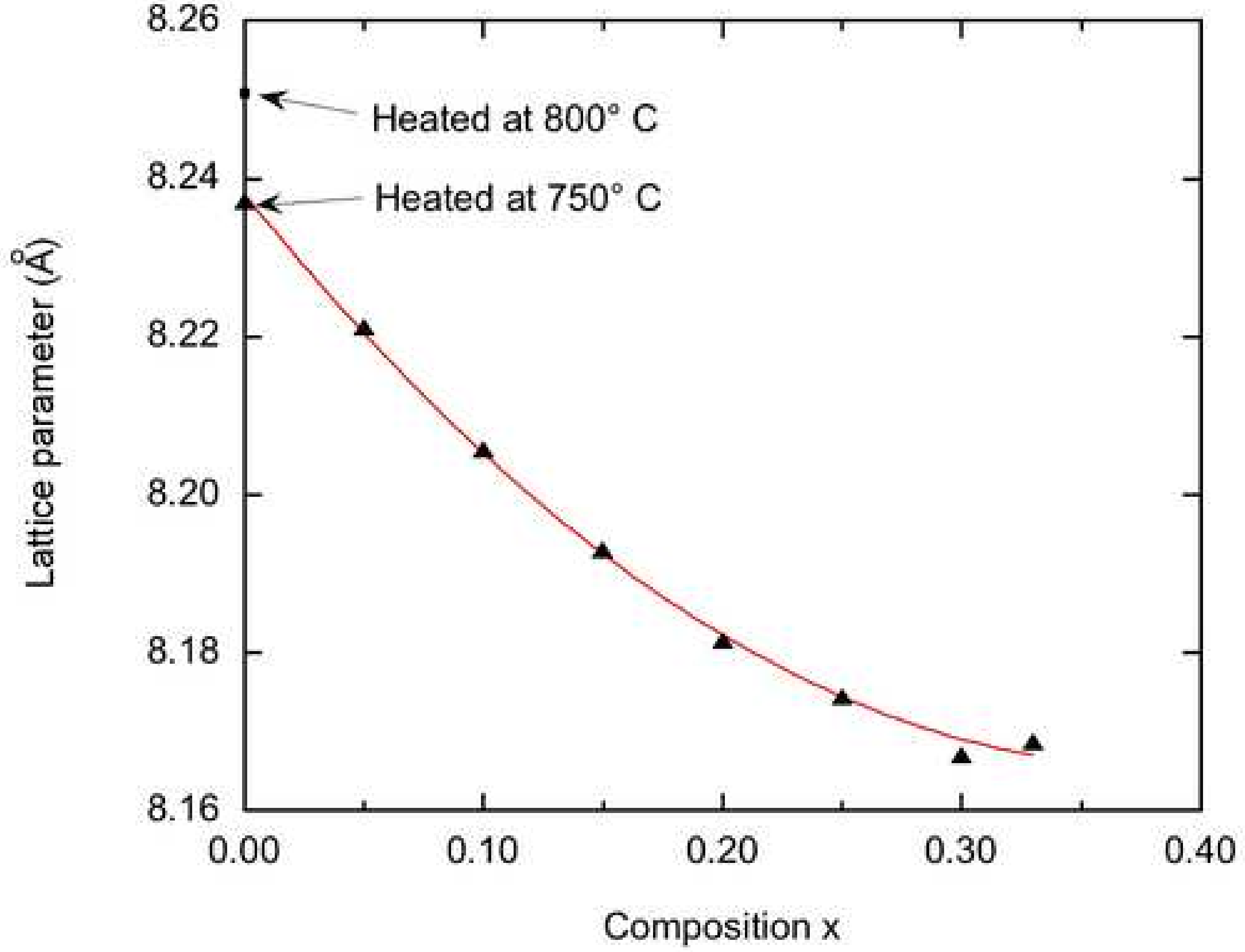
Heated at 800° C
Heated at 750° C
Lattice parameter (Å)
8.26
8.24
8.22
8.20
8.18
8.16
0.00
0.10
0.20
0.30
0.40
Composition x

Figure3

Figure 3

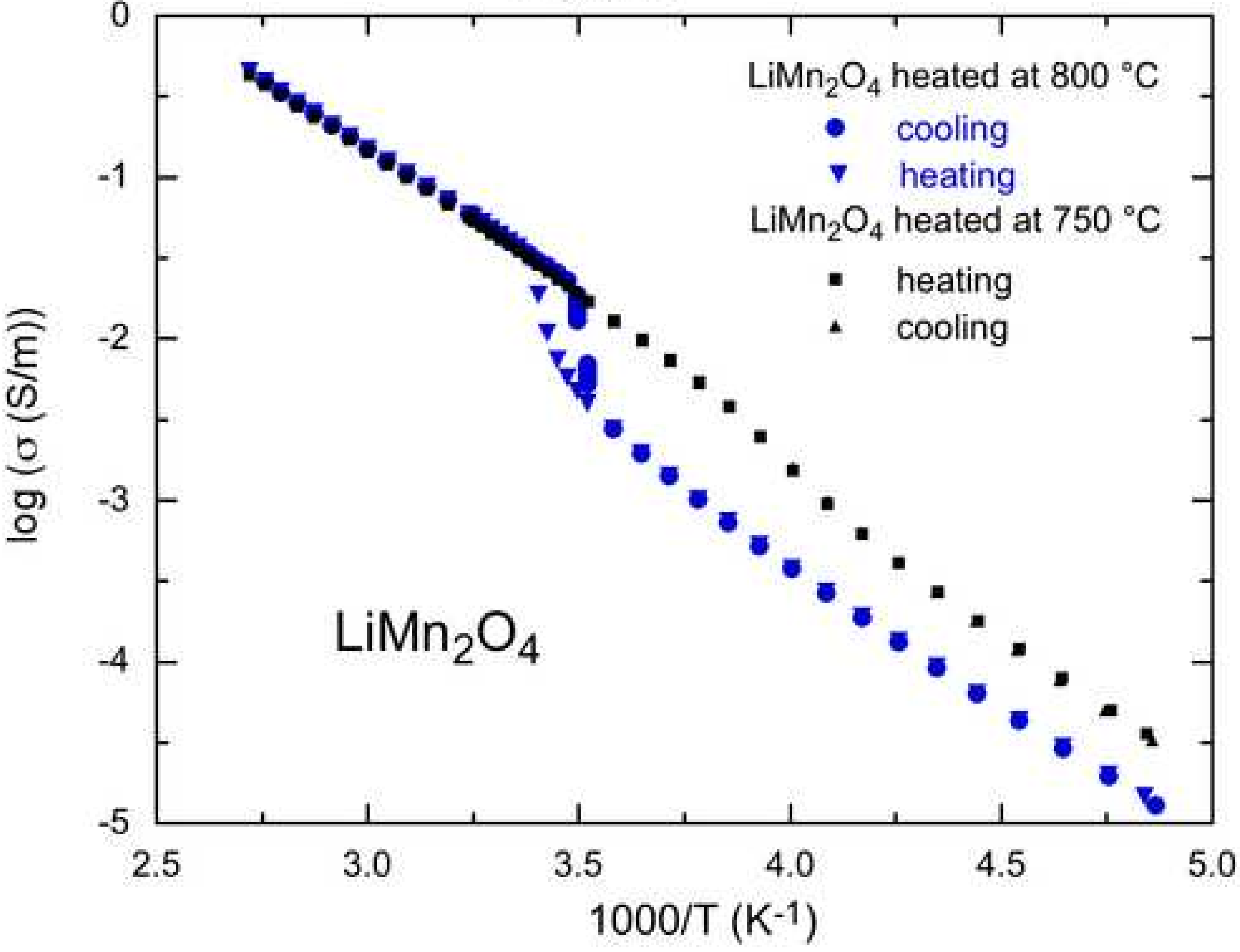

Figure4

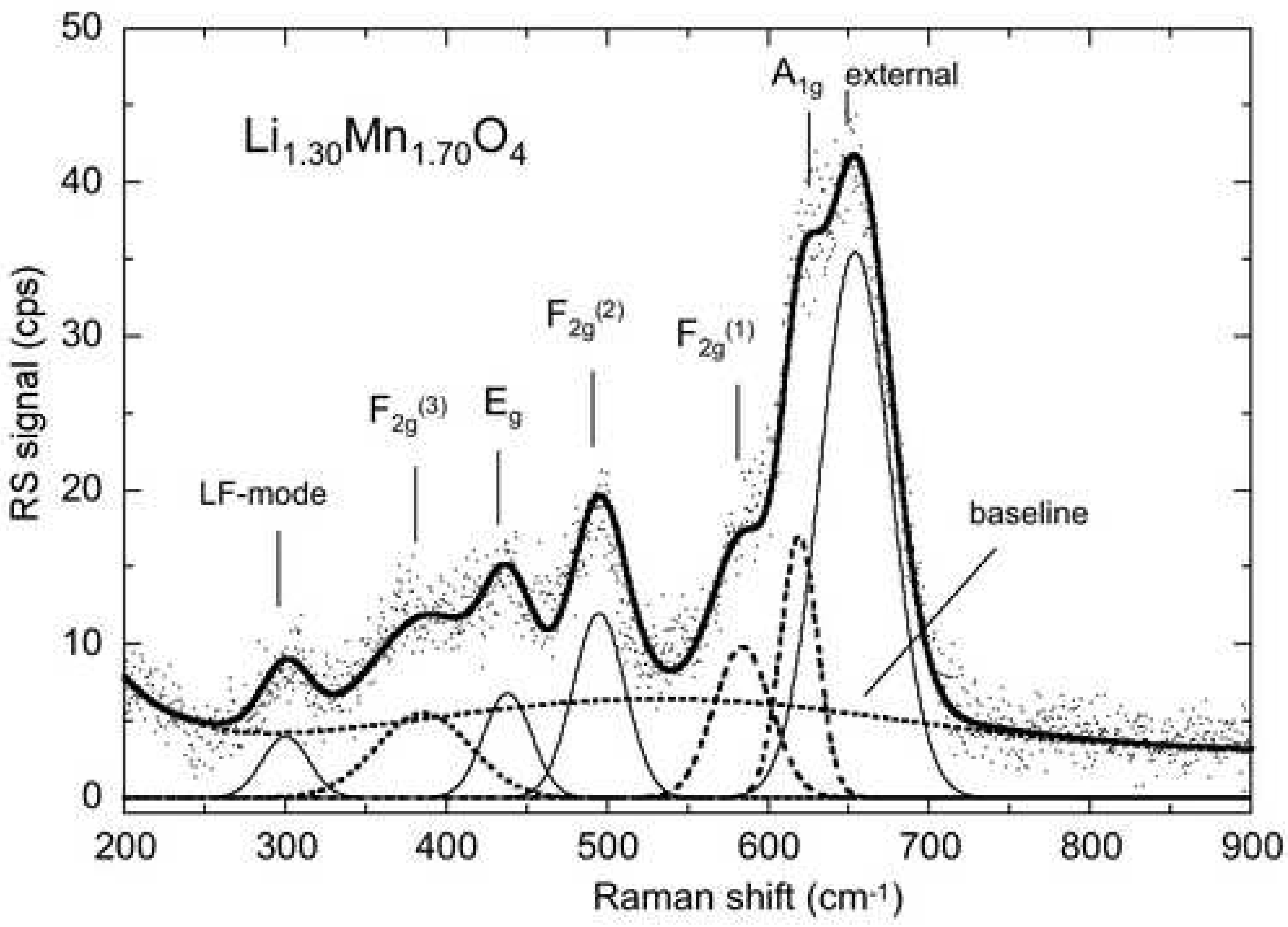
$Li_{1.30}Mn_{1.70}O_4$
RS signal (cps)
Raman shift (cm-1)
LF-mode
$F_{2g}^{(3)}$
E_g
$F_{2g}^{(2)}$
$F_{2g}^{(1)}$
A_{1g}
external
baseline
0
10
20
30
40
50
200
300
400
500
600
700
800
900

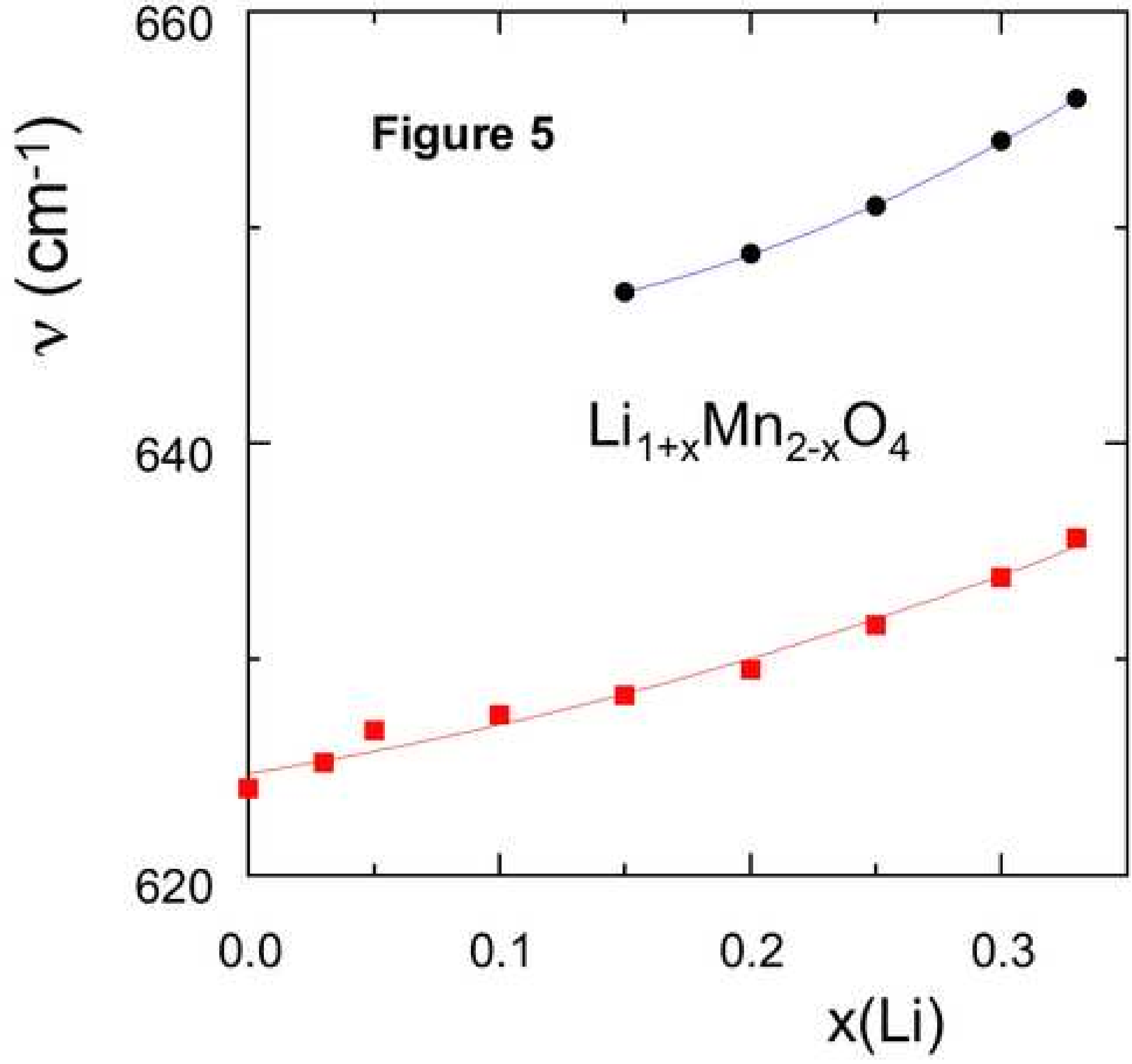
660
640
620
ν (cm-1)
0.0
0.1
0.2
0.3
x(Li)
Figure 5
$Li_{1+x}Mn_{2-x}O_4$

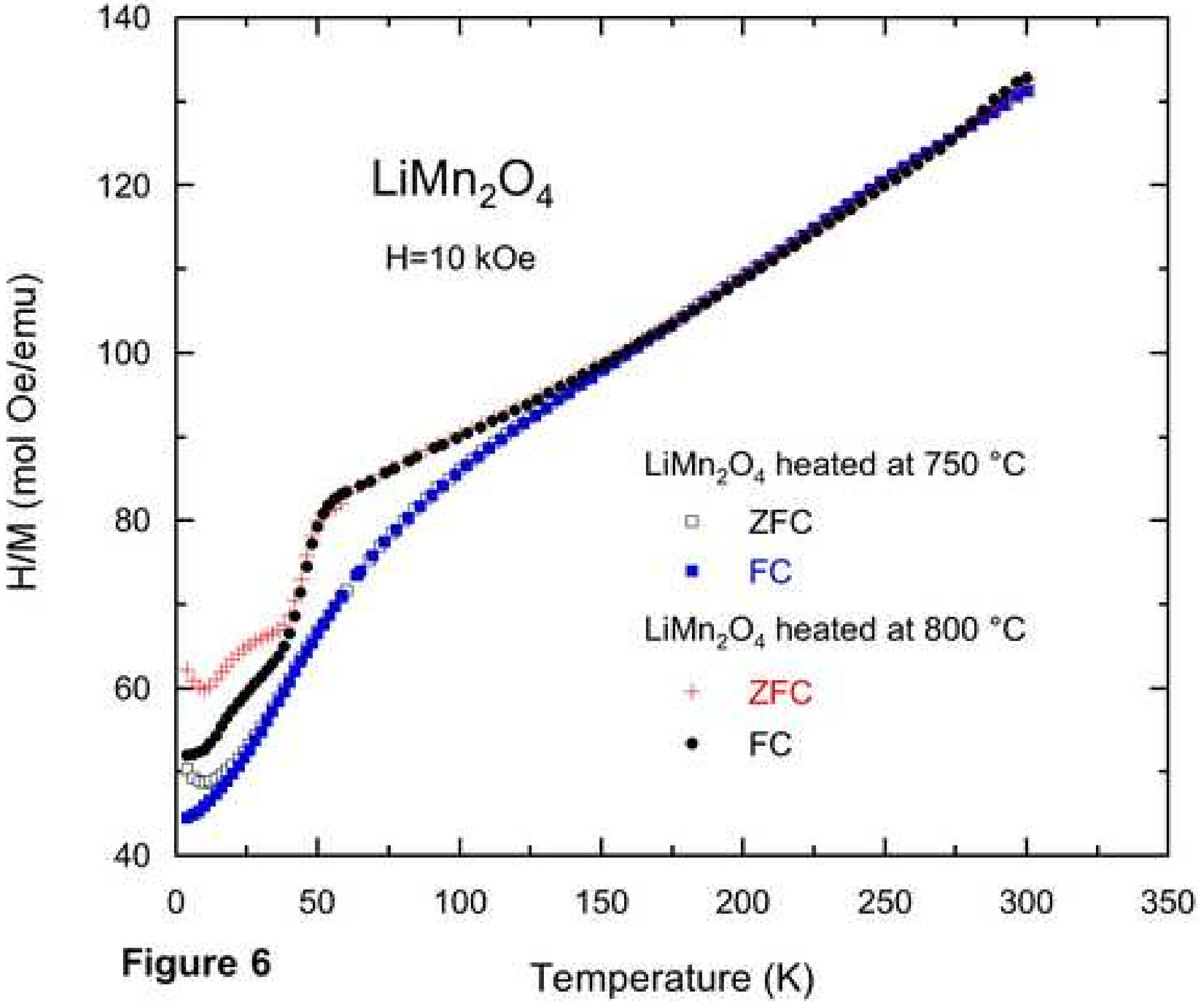

$LiMn_2O_4$
H=10 kOe
$LiMn_2O_4$ heated at 750 °C
□ ZFC
■ FC
$LiMn_2O_4$ heated at 800 °C
+ ZFC
● FC
H/M (mol Oe/emu)
Temperature (K)
40
60
80
100
120
140
0
50
100
150
200
250
300
350

Figure 6

Figure7

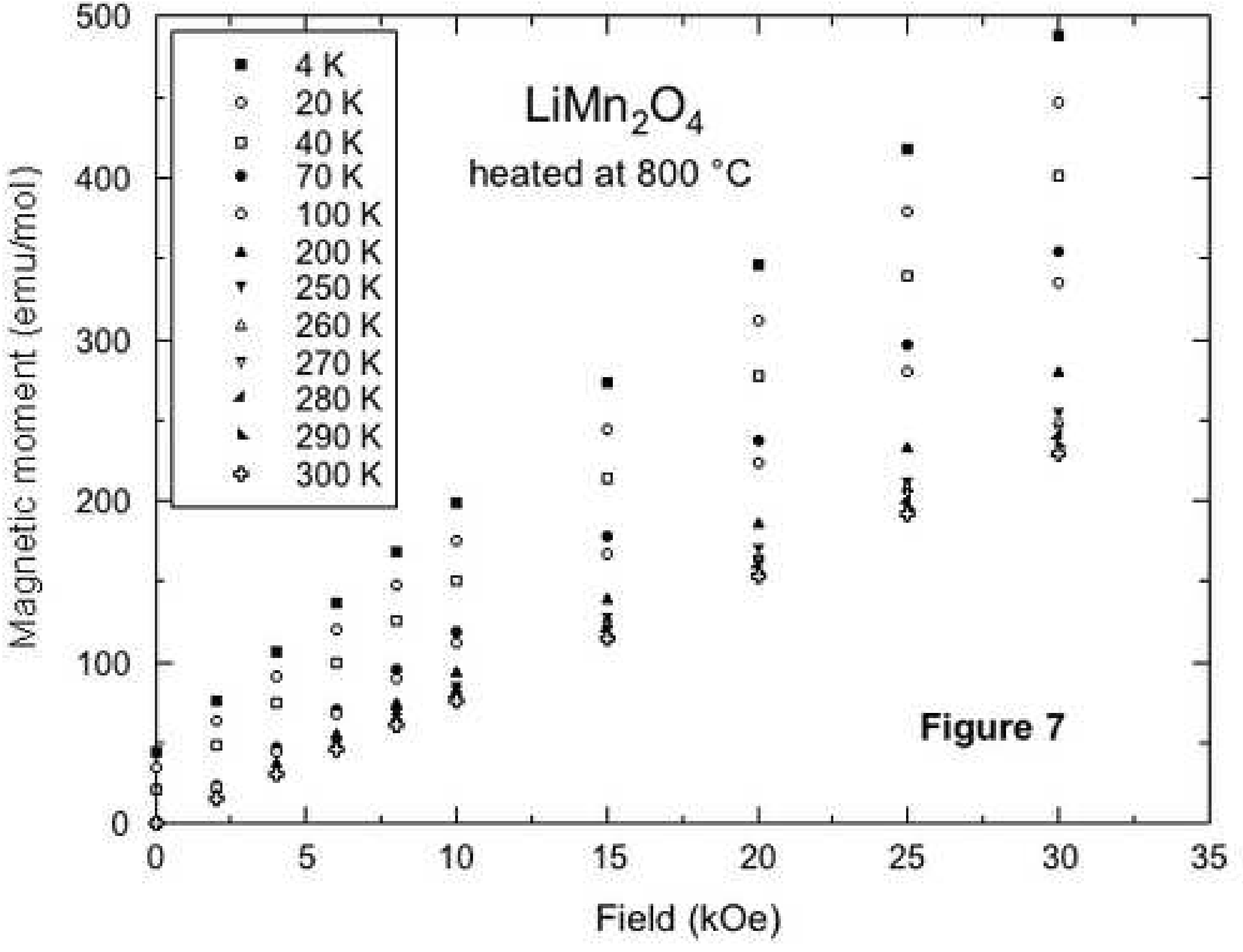
■ 4 K
○ 20 K
□ 40 K
● 70 K
○ 100 K
▲ 200 K
▼ 250 K
△ 260 K
▽ 270 K
◢ 280 K
◣ 290 K
✧ 300 K
$LiMn_2O_4$
heated at 800 °C
Figure 7
Magnetic moment (emu/mol)
0
100
200
300
400
500
Field (kOe)
0
5
10
15
20
25
30
35

Figure8

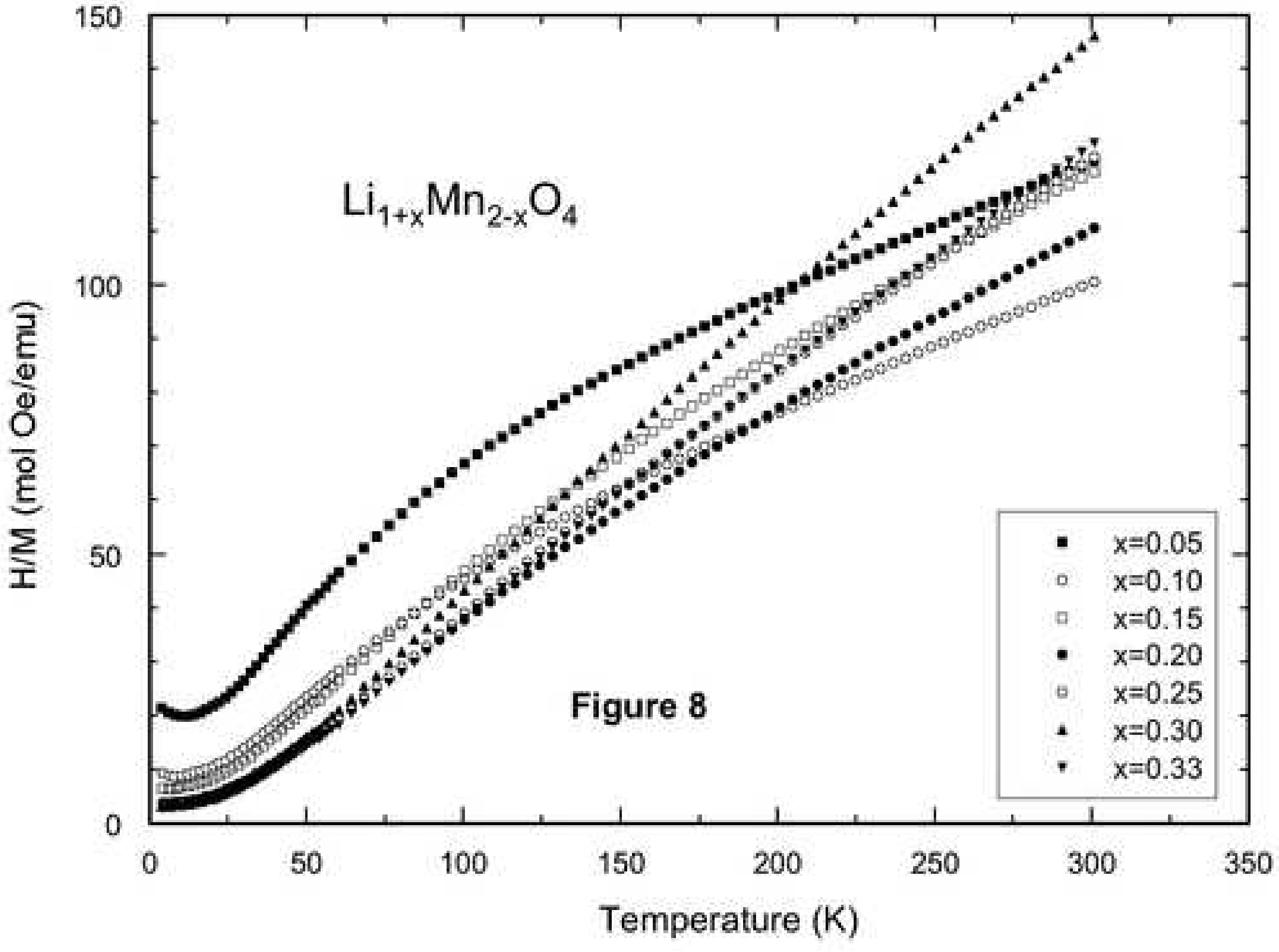

$Li_{1+x}Mn_{2-x}O_4$
Figure 8
H/M (mol Oe/emu)
Temperature (K)
0
50
100
150
0
50
100
150
200
250
300
350
x=0.05
x=0.10
x=0.15
x=0.20
x=0.25
x=0.30
x=0.33

Figure9

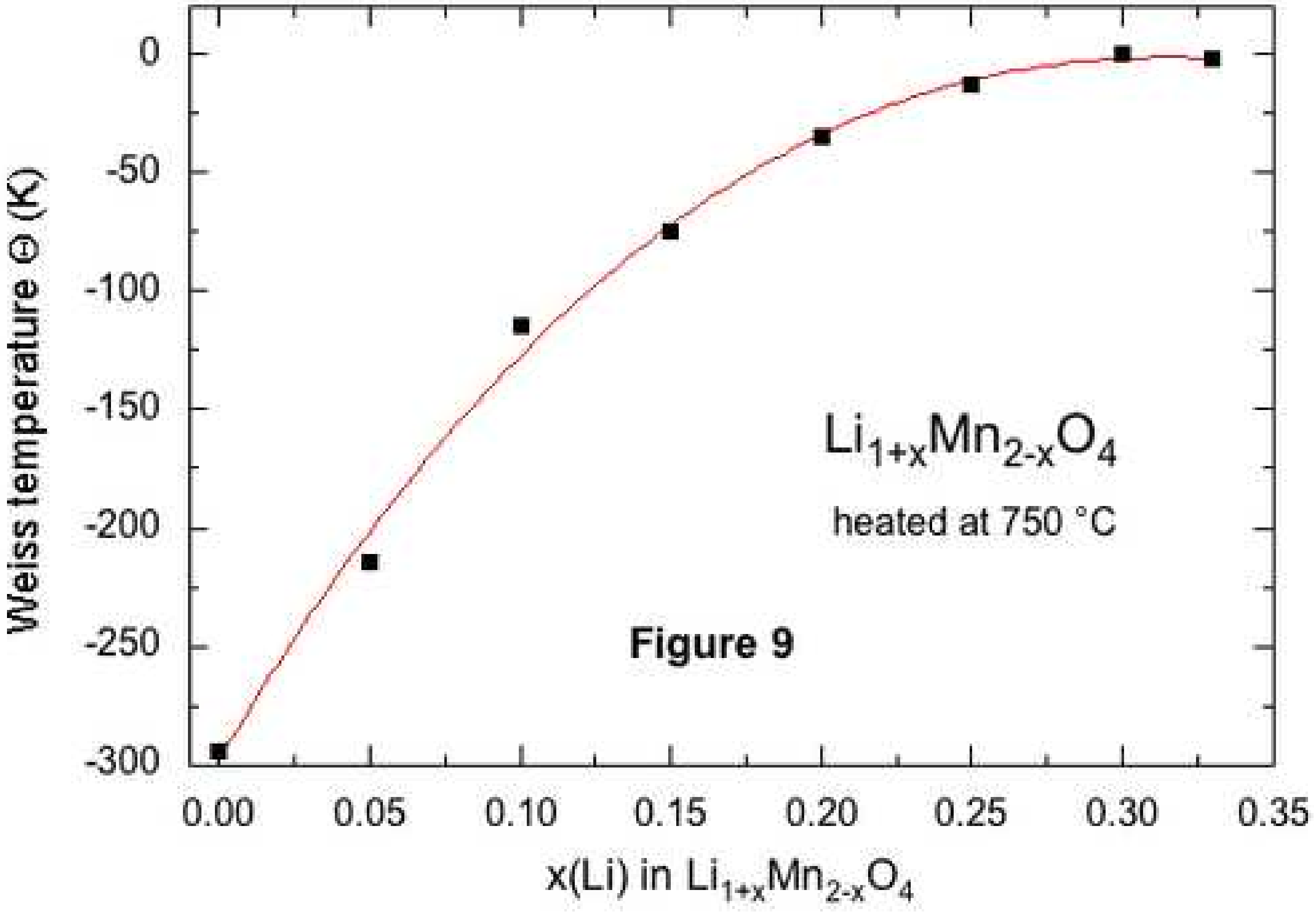
0
-50
-100
-150
-200
-250
-300
Weiss temperature Θ (K)
0.00
0.05
0.10
0.15
0.20
0.25
0.30
0.35
x(Li) in $Li_{1+x}Mn_{2-x}O_4$
$Li_{1+x}Mn_{2-x}O_4$
heated at 750 °C
Figure 9

Figure10

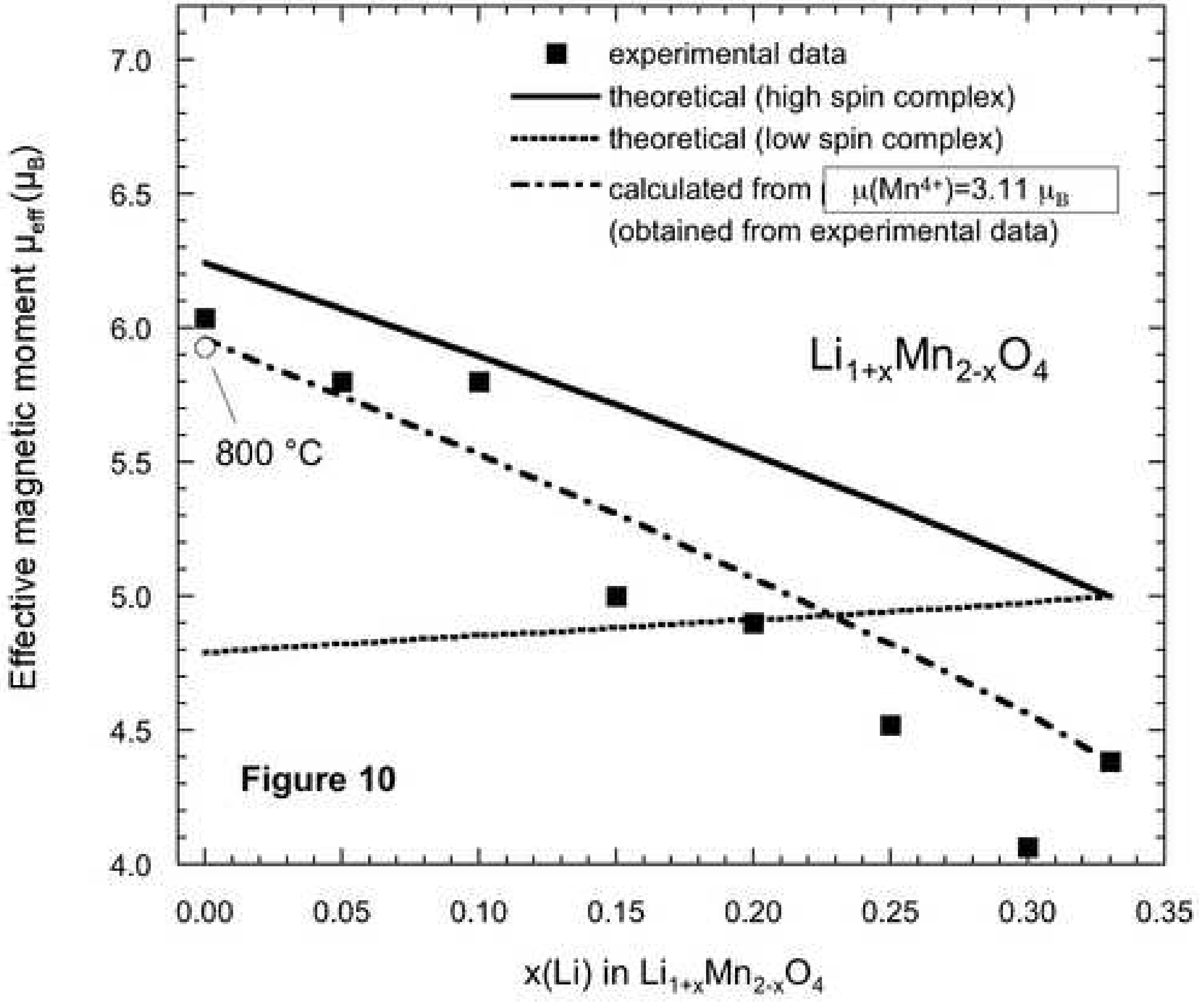
experimental data
theoretical (high spin complex)
theoretical (low spin complex)
calculated from μ(Mn4+)=3.11 μB
(obtained from experimental data)
Li1+xMn2-xO4
800 °C
Figure 10
Effective magnetic moment μeff (μB)
7.0
6.5
6.0
5.5
5.0
4.5
4.0
0.00
0.05
0.10
0.15
0.20
0.25
0.30
0.35
x(Li) in Li1+xMn2-xO4

Figure11

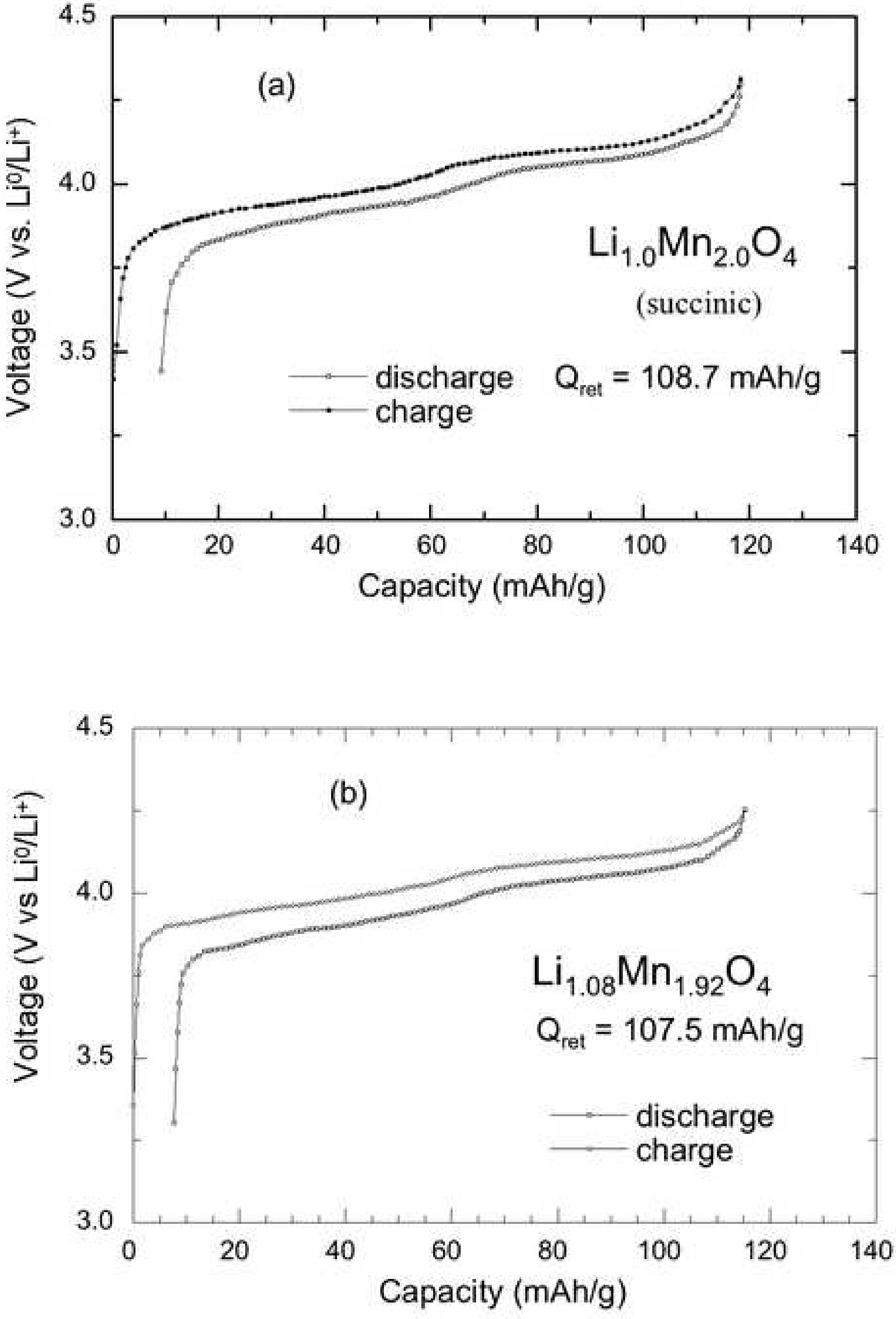
(a)
Voltage (V vs. Li^0/Li$^+$)
4.5
4.0
3.5
3.0
0
20
40
60
80
100
120
140
Capacity (mAh/g)
$Li_{1.0}Mn_{2.0}O_4$
(succinic)
discharge
charge
Q_{ret} = 108.7 mAh/g
(b)
Voltage (V vs Li^0/Li$^+$)
4.5
4.0
3.5
3.0
0
20
40
60
80
100
120
140
Capacity (mAh/g)
$Li_{1.08}Mn_{1.92}O_4$
Q_{ret} = 107.5 mAh/g
discharge
charge

Figure12

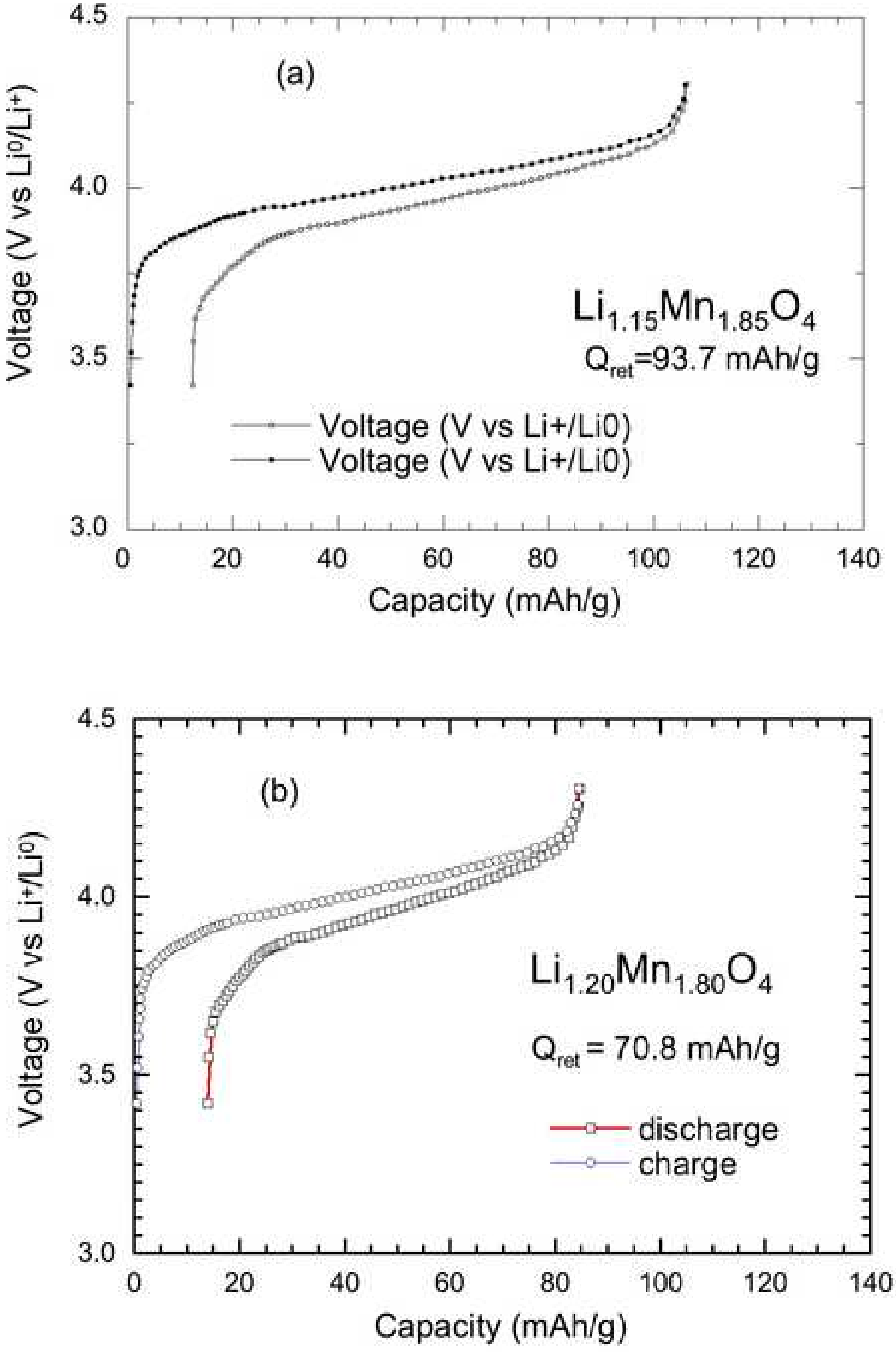
(a)
Voltage (V vs Li^0/Li^+)
4.5
4.0
3.5
3.0
0
20
40
60
80
100
120
140
Capacity (mAh/g)
$Li_{1.15}Mn_{1.85}O_4$
Q_{ret}=93.7 mAh/g
Voltage (V vs Li+/Li0)
Voltage (V vs Li+/Li0)
(b)
Voltage (V vs Li^+/Li^0)
4.5
4.0
3.5
3.0
0
20
40
60
80
100
120
140
Capacity (mAh/g)
$Li_{1.20}Mn_{1.80}O_4$
Q_{ret} = 70.8 mAh/g
discharge
charge